

Received September 9, 2021, accepted September 16, 2021, date of publication September 24, 2021, date of current version October 4, 2021.

Digital Object Identifier 10.1109/ACCESS.2021.3115508

# Inertial-Sensor-Based Non-Dead Reckoning Localization for Ground Vehicles

JUHUI GIM<sup>1</sup>, (Student Member, IEEE), AND CHANGSUN AHN<sup>1</sup>, (Member, IEEE)

School of Mechanical Engineering, Pusan National University, Busan 46241, South Korea

Corresponding author: Changsun Ahn (sunahn@pusan.ac.kr)

This work was supported by the National Research Foundation of Korea by the Ministry of Science and ICT under Grant NRF-2019R1A2C1003103.

**ABSTRACT** This paper proposes an inertial sensor-based positioning method without using dead reckoning. The basic concept estimates the current position based on a pre-indexed map composed of spectrograms of road shapes estimated using inertial sensor signals. The proposed positioning algorithm has three characteristics: a feature-indexed map, the Kalman filter for signal fusion, and the interacting multiple model to integrate multiple maps. The positioning algorithm shows higher positioning accuracy and shorter computing time than a simple scanning method. Furthermore, the size of the map does not proportionally increase as the total length of the road increases. Therefore, the proposed positioning algorithm can be used as a complementary or alternative positioning method to GPS-based positioning methods using only an inertial sensor that is cheap and reliable.

**INDEX TERMS** Feature-indexed map, inertial sensor, localization, non-dead reckoning, road shape estimation, spectrogram.

## I. INTRODUCTION

Vehicle self-positioning is essential for safe autonomous driving [1]–[4]. The most general positioning system is the Global Navigation Satellite System (GNSS), which provides information on the absolute position signals from at least four satellites, and users can easily access the position information with low-cost devices. However, GNSS accuracy could degrade to tens of meter-level depending on the received conditions and direct visibility from the satellites to the devices [5], [6].

Some methods to improve the accuracy of GNSS have been developed, including the Differential Global Positioning System (DGPS) [7] or Real-Time Kinematic (RTK) [8], [9], but they are too expensive to apply to production vehicles and even useless if GPS is completely blocked. A map-based positioning method using vision sensors is another method to increase GNSS accuracy and an alternative to GNSS when GNSS is unavailable. Vision sensors, such as cameras and LIDARs, measure surrounding environments. Vehicles estimate their position using distinguishable features, such as 3-D landmarks [10]–[19] or road markings [20]–[23], extracted from the observations by comparing with a pre-indexed map.

The associate editor coordinating the review of this manuscript and approving it for publication was Pinjia Zhang<sup>1</sup>.

The benefit of this concept is that distinguishable features can be defined from the visual observations intuitively, and accuracy can be higher than that of GNSS without error accumulation [24]–[26]. However, vision sensors have their own detection range limitations, and they are also vulnerable to environmental changes, such as lighting and weather conditions [27]. Vehicle-to-everything (V2X) technology was recently suggested as a robust solution to obtain information about the driving environment and is less vulnerable to visibility and environmental changes. However, the availability and reliability of V2X depend on the communication conditions [28], [29].

If any availability for all signals disappears, e.g., blocked GPS, observation interference of vision sensors, and adverse V2X communication, a new backup sensor for positioning is required. An inertial sensor can be the backup sensor because it measures the vehicle states, not visual objects or communication signals. Therefore, the inertial sensor is less dependent on visibility or communication conditions. Furthermore, inertial sensors are mounted on most vehicles for safety features. The most typical positioning method using inertial sensors is a dead reckoning that estimates the relative position by integrating vehicle states [30]–[32]. However, the dead reckoning method becomes inaccurate due to error accumulation when used for a long-time horizon.

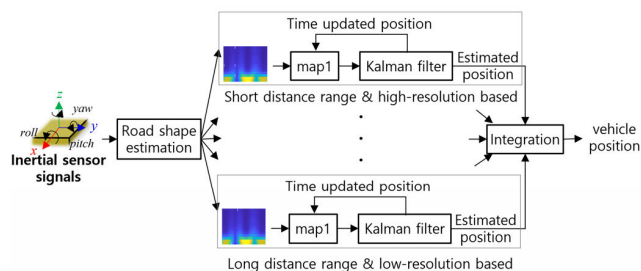


FIGURE 1. Concept of the inertial-sensor-based positioning algorithm.

Some researchers have applied a map-based positioning method using only inertial sensors, not a dead reckoning-based positioning method [33]–[39]. The basic hypothesis of this method is that the inertial sensor signals imply vehicle responses to the road surface profile and the same road surface profile excites similar vehicle motions. In other words, the inertial sensor signals in the distance domain can be the distinguishable features of positions. Pitch rate signals are mainly used for positioning [33]–[37], but roll rate signals are also used [38]. The proposed map-based approaches eliminate the error accumulation problem. However, inertial sensor signals depend on vehicle dynamics and speed ranges. Li *et al.* [36] proposed a braking-robust positioning method using the fact that drivers brake before passing speed bumps. Nevertheless, signal-based approaches are vulnerable to various driving patterns and require long driving distance queries to converge the positioning; for example, braking and pitch rate-based positioning methods require at least 255.40 m for convergence [36]. This long-distance query requires a huge computing load and a huge map size.

A previous study by the authors proposed a map matching-based positioning method using the estimated road profile from the IMU sensor [39]. The study presented how to estimate vertical road shape, demonstrated the repeatability of the vertical road shape at any vehicle type and speed ranges, and showed the possibility of positioning using the road shape spectrogram. This method has many advantages, such as low cost, no error accumulation, and its use as a possible backup or alternative when other positioning methods are unavailable regardless of the vehicle types or speed ranges. However, this method still needs improvements for practical implementation, such as reducing computational load, increasing consistency of positioning accuracy, and simultaneously increasing resolution and robustness.

This paper proposes an inertial-sensor-based non-dead reckoning positioning algorithm that can be applied in practice by realizing low computational load, consistent positioning accuracy, and high resolution and robustness. The inertial sensor signals in the time domain are mapped to vertical and lateral road shapes in the distance domain. From the estimated road shapes, a spectrogram is constructed, which becomes the feature for positioning. The spectrogram-based feature requires a shorter distance for positioning than the time-based

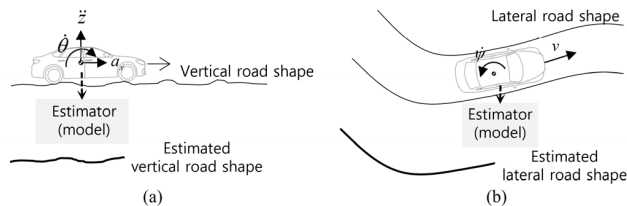


FIGURE 2. Road shape estimation: (a) vertical road shape estimation and (b) lateral road shape estimation.

feature [37], [39]. The proposed algorithm using the road shape spectrogram consists of three remedies: constructing a feature-indexed map; integrating the map-based positioning method and vehicle dynamics using the Kalman filter framework; and, using multiple maps generated using different condition-based spectrograms. Fig. 1 shows the concept of the proposed positioning algorithm. The algorithm shows consistent accuracy with a manageable computational load and map size.

Sections are organized as follows: Section II briefly reviews a method to estimate road shapes, explains a positioning algorithm based on a position-indexed map as a baseline algorithm, and discusses the issues of the positioning algorithm using the position-indexed map. Section III proposes a positioning method using a feature-indexed map, and Section IV shows the algorithm validation. Finally, Section V presents the conclusions.

## II. ROAD SHAPE ESTIMATION AND POSITIONING WITH POSITION-INDEXED MAP

Estimation of road shapes is the first step in inertial-sensor-based positioning. Two types of road shapes are estimated using inertial sensor signals: vertical road shape and lateral road shape, as shown in Fig. 2. The estimated road shapes are signals mapped into the distance domain. The features for map-based positioning are the spectrograms of the estimated road shapes. Usual spectrograms are representations of signals with respect to the time-frequency domain, but we generate spectrograms with respect to the distance-frequency domain to keep a distance index in the feature. The current position information can be extracted by scanning a current spectrogram through the pre-indexed map.

The pre-indexed map can be constructed using the road shapes measured or estimated in the distance domain, not in the time domain. The spectrograms based on the distance-frequency domain become a pre-indexed map. Spectrogram-based features are more robust than one dimension-based feature because spectrograms have spectral characteristics as well as spatial features, and noisy signals are easily removed. An example of a constructed map is shown in Fig. 3.

### A. VERTICAL ROAD SHAPE ESTIMATION

Vehicle dynamic responses with respect to the vertical road shape appear in the pitch rate and vertical acceleration

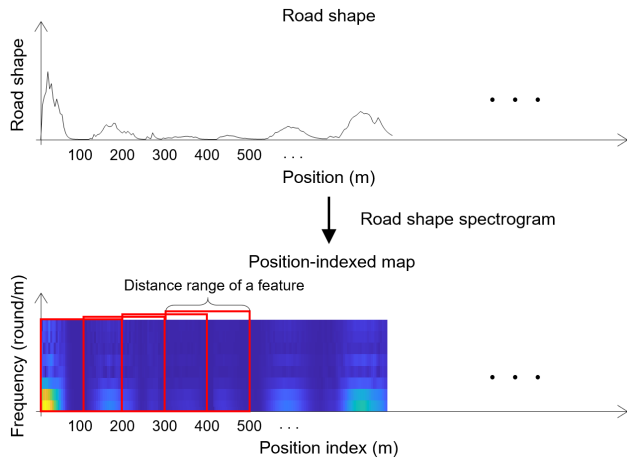


FIGURE 3. Road shape-based map construction.

signals, as shown in Fig. 2 (a). An estimator for the vertical road shape was proposed in a previous paper [39]. The estimator was designed using an unknown input Kalman filter framework that estimates a time-varying unknown input [40], [41]. Common assumptions in unknown input estimation are that the unknown input is constant or cyclic. However, the vertical road shape varies too rapidly to be assumed constant and does not have a simple cyclic pattern. The unknown input Kalman filter estimates the rapidly time-varying unknown input without the assumption of constant or cyclic input at the cost of a one-step delay in estimation.

The designed model for the vertical road shape estimator is based on a half-car model with nonlinear dampers. The model included a sensor bias model to compensate for sensor installation errors and sensor offset. The designed vertical road shape estimator, including the bias model, is applicable for any inertial sensor with different bias conditions. Virtual measurement signals were also introduced to guarantee observability. The designed estimator provided the one-step delayed vertical road shape using the pitch rate, vertical acceleration, and longitudinal acceleration signals, which can be obtained from an inertial sensor.

**B. LATERAL ROAD SHAPE ESTIMATION**

The main signal of vehicle dynamic responses with respect to the lateral road shape is the yaw rate, as shown in Fig. 2 (b). The lateral road shape, or road curvature,  $\rho$ , can be derived as follows:

$$\rho = \frac{\partial \psi}{\partial s} = \frac{\partial \psi / \partial t}{\partial s / \partial t} = \frac{\dot{\psi}}{v}, \tag{1}$$

where  $\psi$  is the vehicle yaw angle,  $\dot{\psi}$  is the yaw rate,  $s$  is the travel distance, and  $v$  is the longitudinal vehicle velocity.

**C. TRANSFORMATION OF ROAD SHAPES TO SPECTROGRAM**

The estimated road shapes are transformed into the distance-frequency domain-based spectrogram. The size of the

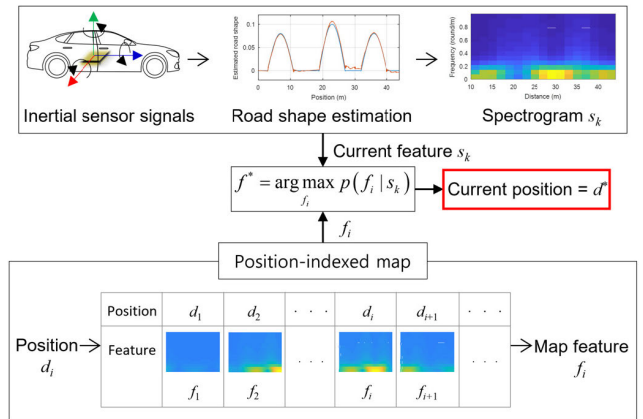


FIGURE 4. Extraction of positioning information using a position-indexed map (scanning method).

spectrogram consists of the frequency and the distance ranges. The frequency range is fixed to under 1 round/m for the vertical road shape and under 0.5 round/m for the lateral road shape. The distance range of the spectrogram determines the richness of a feature in the spectrogram. A larger-sized spectrogram would have a higher positioning accuracy but at the expense of computational load.

**D. POSITIONING WITH POSITION-INDEXED MAP**

The map for positioning consists of the same-sized spectrograms indexed by positions. The map works as a function. The input of the function is a position,  $d_i$ , and the output is the corresponding feature (spectrogram),  $f_i$ :

$$f_i = \text{Map}_{PIM}(d_i). \tag{2}$$

Fig. 4 shows a simple scanning method proposed to show that positioning with the position-indexed map (PIM) is possible. The scanning method calculates similarities between the spectrogram measured at the current position and the spectrograms for all positions in the map. Thus, the position of the spectrogram with the highest similarity becomes the estimated current position.

**E. ISSUES OF POSITIONING WITH POSITION-INDEXED MAP**

Fig. 5 shows the estimated vertical and lateral road shapes using inertial sensor signals. The estimated shapes show consistency, even if the inertial sensor signals are measured in different vehicles running at different velocities, which addresses the possibility of localization regardless of the vehicle speed and vehicle dynamics. Fig. 6 shows the spectrograms transformed from the estimated shapes. The size of the spectrogram of the vertical road shape is 1.0 round/m  $\times$  300 m, and the size of the spectrogram of the lateral road shape is 0.5 round/m  $\times$  300 m. These spectrograms are constructed with a series of signal chunks. Each signal chunk consists of signals for a 10-meter distance and is sampled every 0.5 meters. Therefore, each chunk has 95% overlapping

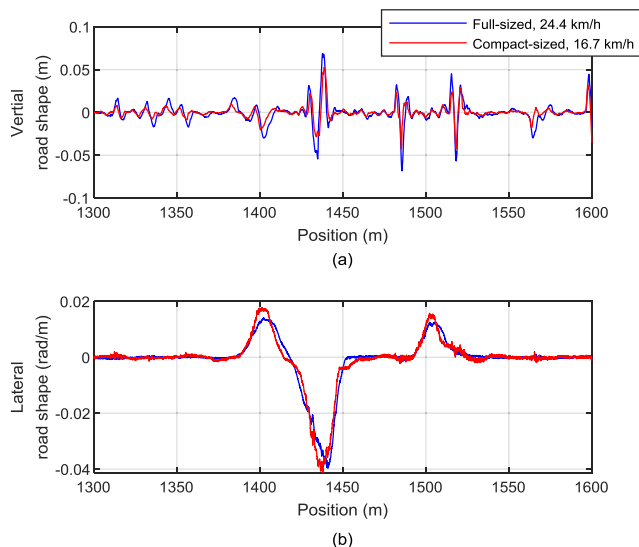


FIGURE 5. Estimated road shapes: (a) estimated vertical road shape and (b) estimated lateral road shape.

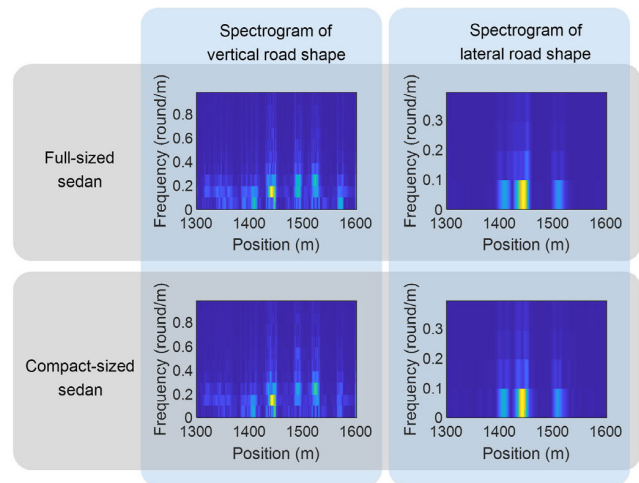


FIGURE 6. Road shape-based spectrograms in the distance and frequency domain.

signals with the neighbor chunks. In Fig. 6, the spectrograms of road shapes are consistent even though the spectrograms were extracted from different vehicle classes running at different speeds.

Fig. 7 shows the positioning result using the simple scanning method. The maps were generated with data from a full-sized sedan driven at 25 km/h. The test vehicle for positioning was a compact-sized sedan running at about 16 km/h. The red dots are the estimated positions with only vertical road shape-based map and black dots only lateral road shape-based map. The positioning results show that the position can be estimated using only inertial sensor signals without an error accumulation problem. However, estimating positions using the scanning method has some issues. Firstly, map scanning is computationally expensive, and the size of the map proportionally increases as the total length of the

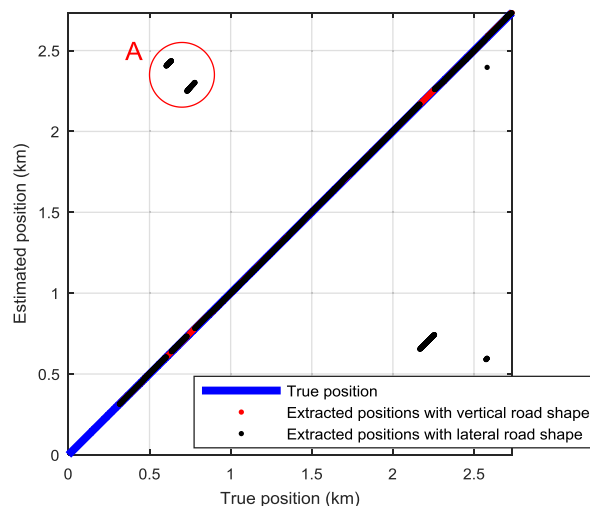


FIGURE 7. Positioning results using the scanning method.

road increases. A map that is too large is problematic for data storage and computational load.

Secondly, the accuracy is extremely degraded in some positions, as highlighted by the red circle (depicted as Circle A) in Fig. 7. This phenomenon occurs because the current position is estimated without considering the past position of the vehicle. It is expected that the positions of the vehicle will be estimated as a gradually changing variable because the features gradually change in their neighboring area. However, a feature on a map is not necessarily unique, and the map-based matching method is a kind of algebraic function. Therefore, the simple algebraic matching function can cause a huge estimation error for a slight difference in the spectrograms.

What happened in the case highlighted in Circle A is presented in Fig. 8. When the vehicle was at 605.49 m, the estimated position was 603.22 m, but when the vehicle moved to 605.99 m, the estimated position was 2405.09 m. This error occurred because the feature measured at 605.99 m has a higher similarity to the map feature of 2405.99 m than those of the neighboring area of 605.99 m. Considering vehicle dynamics, such sudden position changes from 603.22 m to 2405.99 m are not very likely.

Thirdly, the accuracy of the estimated position depends on the chunk size of the spectrogram. Fig. 9 shows positioning examples with spectrograms based on different distance ranges of 100 m, 200 m, 300 m, and 500 m. The results using a longer distance range showed higher accuracy because of the richer features in longer spectrograms. However, the position extraction algorithm requires a higher computational load with a longer range. One possible way to reduce the computational load without reducing the distance range is to reduce the sampling frequency of signal chunks. This approach can increase the richness of features without increasing the computational load but at the cost of degraded resolution in a trade-off relationship.

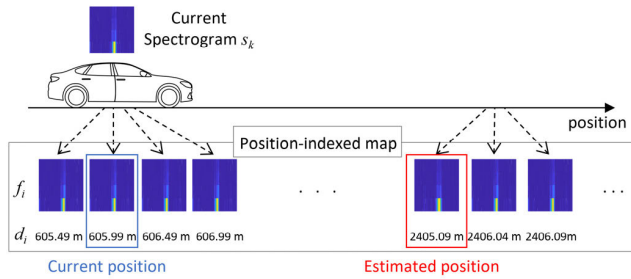


FIGURE 8. A case of a sudden estimated positioning change.

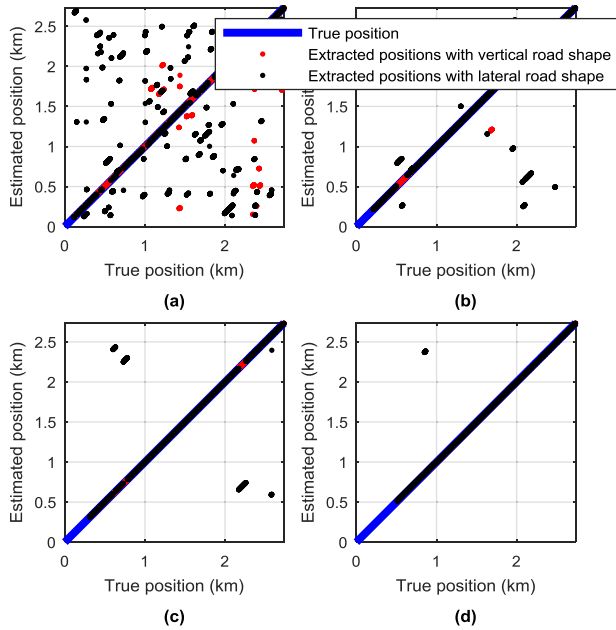


FIGURE 9. Positioning results with several sizes of spectrograms: (a) distance range = 100 m; (b) distance range = 200 m; (c) distance range = 300 m; and (d) distance range = 500 m.

### III. POSITIONING WITH FEATURE-INDEXED MAP

Accuracy and computational load issues are due to the structure of a map and the lack of vehicle dynamics information. Our method is based on an alternative map structure and an estimator framework that fuses positioning results from the maps and vehicle dynamics. A new structure of the map called a feature-indexed map is proposed. It stores the positions and their probabilities with respect to the representative features of spectrograms. Representative features mean the general characteristics of each cluster that groups similar spectrograms. The number of representative features is determined by the desired number of clusters, not by the total length of the road. Therefore, the map requires smaller storage space and less computational load than the position-indexed map.

Furthermore, the feature-indexed map can provide a probability of the estimated position that can be used for further improvement of the positioning accuracy. A positioning algorithm is also designed based on a Kalman filter framework that takes vehicle dynamics into consideration.

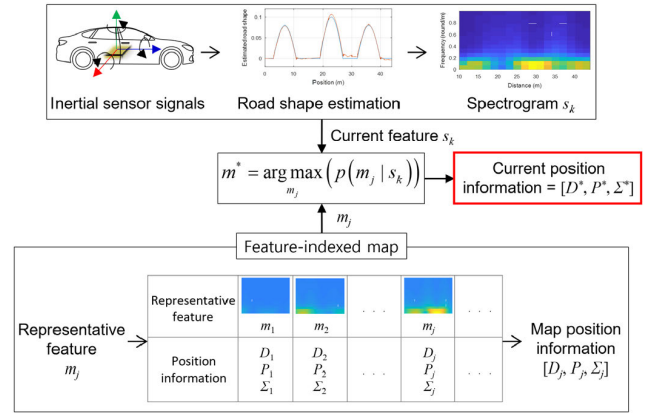


FIGURE 10. Extraction of position information using a feature-indexed map.

Lastly, multiple maps generated using different conditions of spectrograms are used to increase the accuracy without degrading the resolution of the estimation.

#### A. FEATURE-INDEXED MAP

The feature-indexed map (FIM) consists of the positions with their statistical information indexed by representative features. The steps for map construction are: extract the representative features from the same-sized road shape spectrograms, define the position probability distributions of each representative feature, and save the statistical position information of each representative feature. The feature-indexed map works as a function, as shown in Fig. 10. The input of the function is a representative feature,  $m_j$ , and the output is the set of possible positions  $D_j$ , the set of the position probabilities  $P_j$ , and the set of standard deviations  $\Sigma_j$ :

$$[D_j, P_j, \Sigma_j] = \text{Map}_{FIM}(m_j), \quad (3)$$

where  $D_j = \{d_{j1}, d_{j2}, \dots\}$ ,  $P_j = \{p_{j1}, p_{j2}, \dots\}$ , and  $\Sigma_j = \{\sigma_{j1}, \sigma_{j2}, \dots\}$ .

These pieces of information are extracted from the spectrograms. The statistical information is dependent on the definition of representative features. The representative features are defined and identified based on  $K$ -means clustering [42], a centroid-based clustering method that minimizes the squared distances:

$$C^* = \underset{C}{\operatorname{argmin}} \sum_{j=1}^K \sum_{f \in C_j} \|f - m_j\|^2, \quad (4)$$

where  $C = \{C_1, C_2, \dots, C_K\}$ ,  $m_j$  is the center vector of  $C_j$ , and  $f$  is a feature or a spectrogram for the map as the input for  $K$ -means clustering. All  $m_j$  for  $C^*$  are the representative features.

The probability of  $m_j$  being the central vector for the cluster including a given feature  $f_i$  is defined based on the squared

distance between  $m_j$  and  $f_i$ :

$$p(m_j|f_i) = e^{-\|f_i - m_j\|^2} / \sum_{j=1}^K e^{-\|f_i - m_j\|^2}. \quad (5)$$

The likelihood of the feature distribution with respect to a given representative feature is defined as the probabilities of the representative feature with respect to the feature:

$$L(f_i|m_j) = p(m_j|f_i). \quad (6)$$

The probability of a feature with respect to a given representative feature can be defined as a normalized likelihood:

$$p(f_i|m_j) = \frac{L(f_i|m_j)}{\sum_i L(f_i|m_j)}. \quad (7)$$

The feature-indexed map outputs the set of possible positions and their statistical characteristics, so the probability function (7) should be defined with respect to positions, not features. The function is easily re-expressed with respect to positions using the mapping function from a position to a feature, as follows:

$$\begin{aligned} p(m|d) &= p(m|f), & L(d|m) &= L(f|m), \\ p(d|m) &= p(f|m), & f &= \text{Map}_{PIM}(d). \end{aligned} \quad (8)$$

Fig. 11 shows a conceptual image of the probability functions (8). Fig. 12 shows the probability of possible positions for a given cluster  $m_j$  and corresponding statistical information. The local maxima mean the probabilities of possible current positions when the current feature is categorized into the  $j^{\text{th}}$  cluster. We assume that the distribution of the probability around the local maxima is locally Gaussian. The expected values of the Gaussian distributions are the elements of  $D_j$ . The peak values of the Gaussian distributions are the probabilities in  $P_j$ . The standard deviations of the Gaussian distributions are elements of  $\Sigma_j$  and can be used as the measurement error covariance of the estimated position. In other words, the feature-indexed map works as a positioning sensor with Gaussian noise.

### B. KALMAN FILTER-BASED POSITIONING

Once spectrograms are generated using estimated road shapes,  $s_k$ , possible positions and corresponding statistical information are obtained from the feature-indexed map, which is the position information of the most similar representative feature  $m^*$  to the current spectrogram  $s_k$ :

$$[D^*, P^*, \Sigma^*] = \text{Map}_{FIM}(m^*), \quad (9)$$

where

$$\begin{aligned} m^* &= \arg \max_{m_j} (p(m_j|s_k)) \\ &= \arg \max_{m_j} \left( e^{-\|s_k - m_j\|^2} / \sum_{j=1}^K e^{-\|s_k - m_j\|^2} \right). \end{aligned}$$

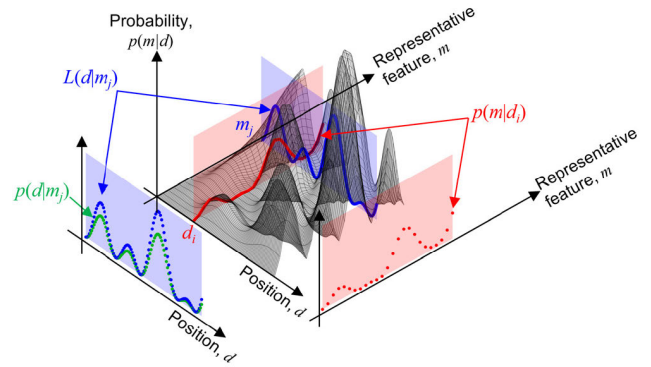


FIGURE 11. Conceptual description of the probability of representative feature for a given position.

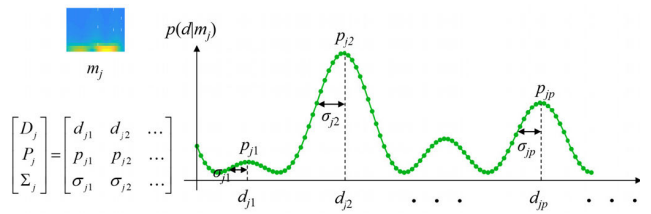


FIGURE 12. Position information of a cluster  $m_j$ .

The current position among the multiple position candidates  $D^*$  is estimated by integrating the probabilistic information of the feature-indexed map and the probable probabilistic information with respect to the previous position using the Kalman filter, as shown in Fig. 13. The estimated positions from the feature-indexed map have Gaussian noises, which guarantees the optimal condition for the Kalman filter.

The system and measurement models for the Kalman filter are designed as follows:

$$\begin{aligned} x_k &= \mathbf{F}x_{k-1} + \mathbf{G}u_{k-1} + w_k, \\ y_k &= \mathbf{H}x_k + n_k, \end{aligned} \quad (10)$$

where

$$\begin{aligned} x_k &= d_k, & u_k &= v_k, \\ F &= 1, & G &= dt, & H &= [1 \quad 1]^T, \\ y_k &= \mathbf{z}_k = [d_{ver,k}^* \quad d_{lat,k}^*]^T, \end{aligned}$$

$d_k$  is the longitudinal position,  $v_k$  is the current velocity, and  $dt$  is the sampling time.  $w_k$  and  $n_k$  are the process and measurement noises assumed to be zero-mean Gaussian white noise with covariance  $\mathbf{Q}_k$  and  $\mathbf{R}_k$ , respectively. The measurement  $\mathbf{z}_k$  is composed of the positions extracted using vertical and lateral road shapes from the map,  $d_{ver,k}^*$  and  $d_{lat,k}^*$ . The Kalman filter estimates the vehicle position through the recursive updates between the time-update using vehicle dynamics and the measurement-update using the measurements from the map [43].

The concept of extracting positions,  $d_{ver,k}^*$  and  $d_{lat,k}^*$ , is shown in the bottom box in Fig. 13, which becomes the

measurement of the Kalman filter. The concept to extract the most probable position among the set of position candidates from the map uses the time-updated state  $\hat{x}_{k|k-1}$  and its error covariance  $\hat{P}_{k|k-1}$  to the probabilistic information of the position candidates. Given a representative feature ( $m_j$ ) and time-updated vehicle position information ( $\hat{x}_{k|k-1}, \hat{P}_{k|k-1}$ ), the probability of the position is expressed as the weighted version of feature-based position probability  $p(d|m_j)$  using vehicle dynamics-based position probability  $p(x|\hat{x}_{k|k-1}, \hat{P}_{k|k-1})$ :

$$p(d|m_j, \hat{x}_{k|k-1}, \hat{P}_{k|k-1}) = p(d|m_j) \cdot p(x|\hat{x}_{k|k-1}, \hat{P}_{k|k-1}), \quad (11)$$

where  $p(x|\hat{x}_{k|k-1}, \hat{P}_{k|k-1})$  is the Gaussian distribution of  $x$  given  $\hat{x}_{k|k-1}$  and  $\hat{P}_{k|k-1}$ .

The most probable position  $d^*$  is the position with the highest probability among the modified position probabilities, which becomes the measurement. The corresponding measurement noise  $\sigma^*$  is the standard deviation of  $d^*$ :

$$\begin{aligned} d_k^* &= \arg \max_d p(d|m_j, \hat{x}_{k|k-1}, \hat{P}_{k|k-1}), \\ \sigma_k^* &= \sigma \text{ of } d_k^*. \end{aligned} \quad (12)$$

The expected positions and standard deviations identified by vertical and lateral road shapes are augmented as the measurement vector  $\mathbf{z}_k$  and covariance matrix  $\mathbf{R}_k$ . The

measurement vector and the noise covariance matrix are:

$$\mathbf{z}_k = \begin{bmatrix} d_{ver,k}^* \\ d_{lat,k}^* \end{bmatrix}, \quad \mathbf{R}_k = \begin{bmatrix} \sigma_{ver,k}^{*2} & 0 \\ 0 & \sigma_{lat,k}^{*2} \end{bmatrix}, \quad (13)$$

where  $d_{ver,k}^*$  and  $d_{lat,k}^*$  are the extracted positions at  $k$  time step using the feature-indexed maps of vertical road shapes and lateral road shapes, respectively.  $\sigma_{ver,k}^*$  and  $\sigma_{lat,k}^*$  are the corresponding standard deviations. The Kalman filter is measurement-updated based on the augmented measurement vector  $\mathbf{z}_k$  and covariance matrix  $\mathbf{R}_k$ .

### C. ACCURACY IMPROVEMENT USING MULTIPLE MAPS AND MULTIPLE INTERACTING FILTERS

The positioning accuracy of the proposed method is dependent on the size of the spectrogram. We propose a method to improve the accuracy with a small increase in computational load while keeping the resolution at the current level. The method is the integration of Kalman filter-based positioning methods using different-sized maps. A Kalman filter-based positioning method with a short-distance map is expected to have the advantage of high resolution, and one with a long-distance map is expected to have the advantage of high accuracy.

The basic idea is adopted from the interaction multiple model (IMM) estimator structure, as shown in Fig. 14. The IMM approach is used to improve the efficiency of an adaptive system by switching or tuning several models based on the responses of the system and models [44]–[47]. The

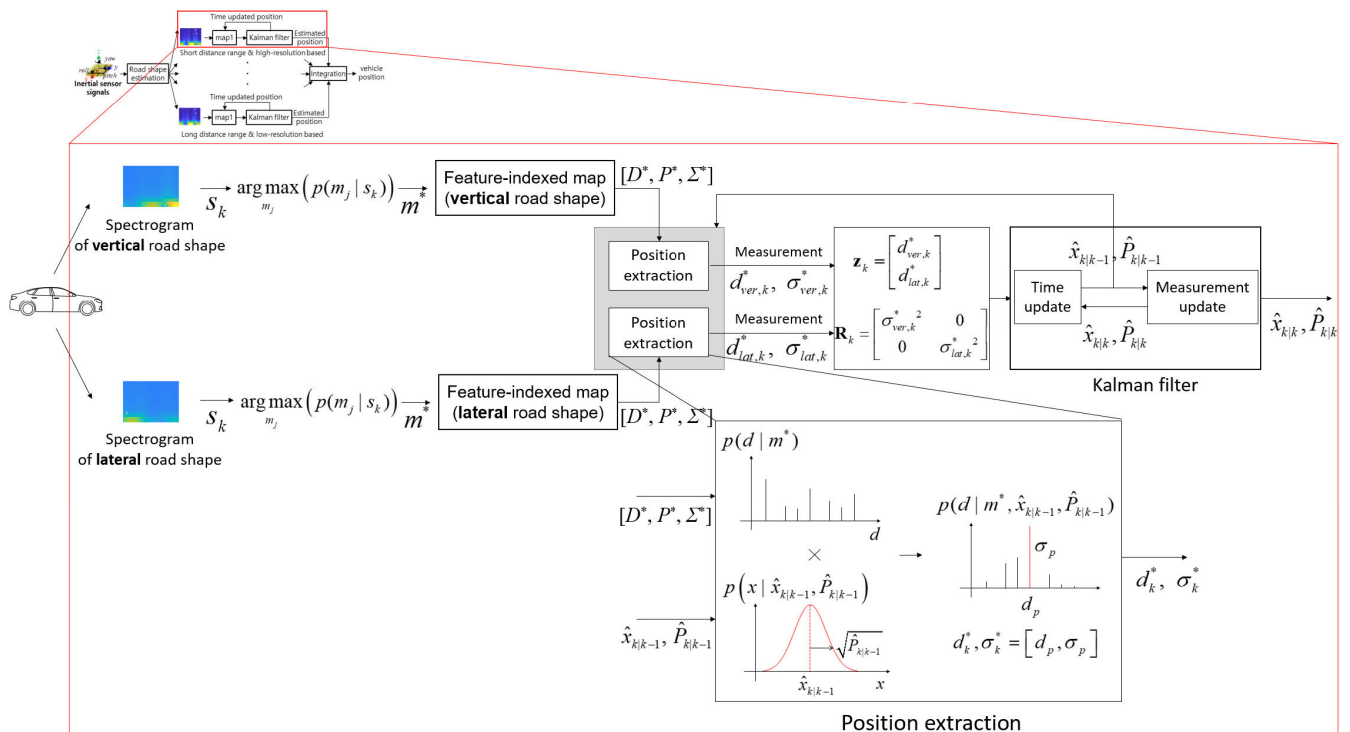


FIGURE 13. Positioning algorithm based on the integration of the Kalman filter and the feature-indexed map.

IMM architecture has three steps: interacting, filtering, and integrating with the updated mode probability.

The interacting step mixes states  $\hat{x}_{k-1|k-1}^i$  and their covariances  $\hat{P}_{k-1|k-1}^i$  of each model with the mixing probability:

$$\mu_{k-1|k-1}^{ji} = \frac{\pi_{ji}\mu_{k-1}^j}{\sum_{j=1}^N \pi_{ji}\mu_{k-1}^j}, \quad (14)$$

where  $\mu_{k-1}^j$  is the posterior mode probability of model  $j$  in step  $k-1$ ,  $\pi_{ji}$  is the prior probability for the transition from model  $j$  to model  $i$ , and  $N$  is the number of models.

The mixed states  $\tilde{x}_{k-1|k-1}^i$  and their covariance  $\tilde{P}_{k-1|k-1}^i$  of model  $i$ , under the Gaussian mixture model assumption, derived as:

$$\begin{aligned} \tilde{x}_{k-1|k-1}^i &= \sum_{j=1}^N \mu_{k-1|k-1}^{ji} \hat{x}_{k-1|k-1}^j, \\ \tilde{P}_{k-1|k-1}^i &= \sum_{j=1}^N \mu_{k-1|k-1}^{ji} \\ &\quad \times \left[ \hat{P}_{k-1|k-1}^j + e_{k-1|k-1}^j \left( e_{k-1|k-1}^j \right)^T \right], \\ e_{k-1|k-1}^j &= \left( \hat{x}_{k-1|k-1}^j - \tilde{x}_{k-1|k-1}^i \right). \end{aligned} \quad (15)$$

These mixed states and their covariance become the initial state and covariance of each Kalman filter-based position estimator constructed with the different conditioned maps. The Kalman filter-based position estimators predict and update their own position and error covariance using the estimated position from each map, respectively.

The estimated results of each Kalman filter are integrated with the updated mode probability based on the innovation  $(z_k^i - \mathbf{H}_k \hat{x}_{k|k-1}^i)$  and its covariance  $S_k^i$  from the Kalman filter. The updated mode probability is expressed as:

$$\mu_k^i = \frac{\mathcal{N}(z_k^i; \mathbf{H}_k \hat{x}_{k|k-1}^i, S_k^i) \sum_{j=1}^N \pi_{ji} \mu_{k-1}^j}{\sum_{l=1}^N \mathcal{N}(z_k^l; \mathbf{H}_k \hat{x}_{k|k-1}^l, S_k^l) \sum_{j=1}^N \pi_{jl} \mu_{k-1}^j}, \quad (16)$$

where  $\mathcal{N}(x; \bar{x}, \sigma^2)$  is the probability of  $x$  given  $\bar{x}$  and  $\sigma^2$  (the mean and the variance of  $x$  under the Gaussian assumption). The updated mode probability is the mode probability-weighted with the estimated position probability from each Kalman filter. The final state  $\hat{x}_{k|k}$  and its covariance  $\hat{P}_{k|k}$ , integrated all states from  $N$  models under the Gaussian mixture model assumption with the updated mode probability, are the final estimated current position and its error covariance:

$$\begin{aligned} \hat{x}_{k|k} &= \sum_{i=1}^N \mu_k^i \hat{x}_{k|k}^i, \\ \hat{P}_{k|k} &= \sum_{i=1}^N \mu_k^i \left[ \hat{P}_{k|k}^i + \left( \hat{x}_{k|k}^i - \hat{x}_{k|k} \right) \left( \hat{x}_{k|k}^i - \hat{x}_{k|k} \right)^T \right]. \end{aligned} \quad (17)$$

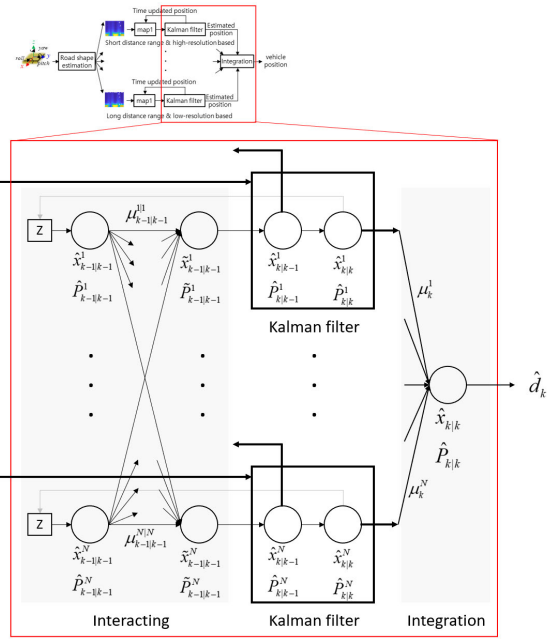


FIGURE 14. Integration of multiple maps using the interacting multiple model framework.

The designed model structures have the same dynamics but different measurements from the different maps. Once a measurement is performed, the transition probabilities from model  $j$  to  $i$  are determined as follows:

$$\pi_{ji} = \begin{cases} 1/N_A, & \text{measurement } i \text{ is available,} \\ 0, & \text{measurement } i \text{ is unavailable,} \end{cases} \quad (18)$$

where  $N_A$  is the total number of models for which measurements are available.

#### IV. ALGORITHM VALIDATION

The proposed algorithm was validated using the data collected on campus roads of a university, as shown in Fig. 15. Two different vehicles were used for the validation: a full-sized sedan and a compact-sized sedan. In general, the road shape map would be pre-defined with the real road shape. However, the consistency of the estimated road shape makes it possible to generate a road shape map using the estimated road shapes with different types of vehicles. The full-sized sedan was used for map construction, and the compact-sized sedan was used to perform positioning. The IMU sensor with the generic specification, consisting of 3-axis accelerometers with 10 g range and 2  $\mu$ g bias, and three gyros with 100  $^\circ$ /s range and 2  $^\circ$ /h bias, was installed near the center of gravity of vehicles.

Two sets of spectrograms from vertical and lateral road shapes were constructed with 10-meter window size, 95% overlap, and a 100-meter distance range for map construction. These two sets of spectrograms are the basis of the feature-indexed map. The number of representative features to construct the feature-indexed map is dependent on the total



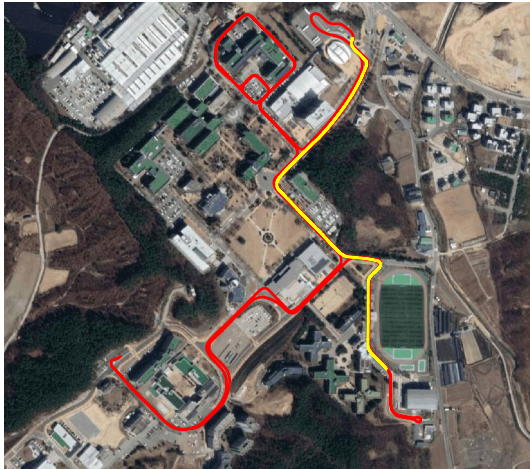


**FIGURE 15.** Test environment: the red line is for map construction, and the yellow line is for the positioning test.

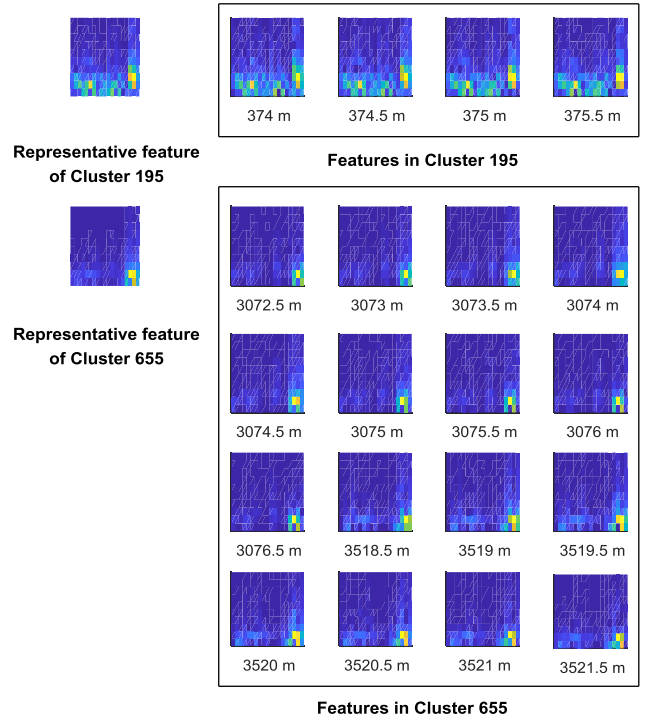
number of spectrograms of the map and affects the resolution and accuracy of the representative feature with a trade-off relationship. We extracted 1000 representative features from each group of spectrograms when the number of spectrograms is 9160.

Fig. 16 shows two representative features for spectrograms of the vertical road shape and the corresponding spectrograms. The spectrograms in the same cluster have high similarities to each feature. However, not all spectrograms are from neighboring areas of a single position. For example, in Cluster 655, some are from 3074 meters, and some are from 3520 meters. Therefore, the possible positions are probabilistically determined.

The probabilities of the representative feature for given positions are shown in Fig. 17 (a). For example, when a current spectrogram is categorized into Cluster 655, the probability of the possible position is distributed, as shown in Fig. 17 (b). In this case, the most likely position would be 3074.5 meters unless any history of vehicle positions is given.

If information about the vehicle position in the previous time step is given, choosing the most likely current position would be different. For example, Fig. 18 (a) shows the positions with their probabilities obtained using only the feature-indexed map. Fig. 18 (b) shows the probability of the estimated position obtained using the Kalman filter. As shown in Fig. 18 (c), combining these two pieces of information, a new estimated position can be determined as 1458 meters, and its variance becomes the measurement noise.

The effect of integration with the Kalman filter is shown in Fig. 19, where the accuracy has been improved by removing the sudden position changes. Figs. 19 (a) and (b) show the positioning results with the scanning method using the position-indexed vertical and lateral shape map, respectively. Fig. 19 (c) shows the positioning result using the integration of the Kalman filter framework and the feature-indexed map that includes both vertical and lateral road shapes. The



**FIGURE 16.** Two examples of the representative feature in a map based on vertical road shape and the chunks of spectrograms corresponding to each representative feature.

process noise covariance is assumed as 50 m. The integration of the Kalman filter framework and the feature-indexed map can remove the sudden position jumps by the scanning method.

The effect of using multiple sizes of maps is shown in Fig. 20. The positioning algorithm uses two feature-indexed maps. The first one consists of spectrograms with a 300-m distance range and 50% overlapping for positioning accuracy ( $i = 1$ , Map 1). The other consists of spectrograms with a 100-m distance range and 95% overlapping for positioning resolution ( $i = 2$ , Map 2). The transition probabilities are:

$$\pi_{ji} = \begin{cases} 1, & \text{for available measurement } i, \\ 0, & \text{for unavailable measurement } i, \end{cases} \quad (19)$$

where  $i = 1, 2$ . When both measurements from Map 1 and Map 2 are available, the transition probabilities are equal for each measurement:

$$\pi_{ji} = 0.5. \quad (20)$$

The blue and red lines in Fig. 20 show the root mean square (RMS) errors of the estimators using single feature-indexed maps. The black line shows the estimator using the two maps. The mean distance error of the estimator with Map 1 was 2.3 m, with Map 2, 3.2 m, and with both Map 1 and Map 2, 1.7 m. The estimator with Map 1 shows higher accuracy than Map 2's because of the larger size of the spectrogram. However, the resolution of the estimator with Map 1 is worse

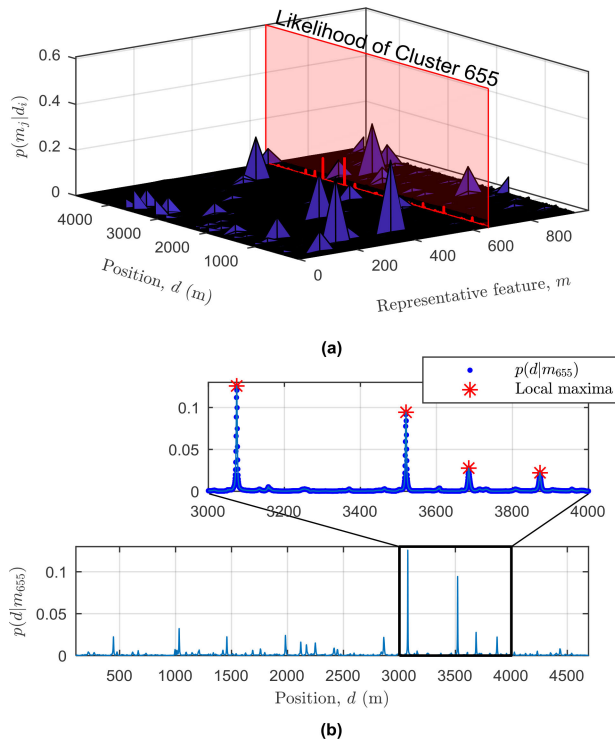


**FIGURE 17.** Probability distributions: (a) probabilities of representative features for given positions and (b) position probability when  $m_{655}$  (the representative feature of Cluster 655) is given.

than Map 2's, as seen in the bottom plot of Fig. 20. The estimator with multiple maps showed higher accuracy than the estimators with single maps. Furthermore, the resolution of the estimator with multiple maps is the same as the highest resolution among the multiple maps.

Fig. 21 compares the map sizes and the computing times of several methods with respect to the total distance of the map, which determines the computational load. The computing time is defined as the averaged calculation time for map matching, i.e., the calculation time for extracting measurement vector  $z_k$  from the map. The blue line is for the scanning method with the position-indexed map (PIM). The red line is for the proposed method that integrates a Kalman filter and multiple feature-indexed maps (Map 1 + Map 2). The black line is for the integrated method of a Kalman filter and a single feature-indexed map, which shows a similar accuracy to the proposed method. All maps were constructed to have the same resolution. A longer total distance of the map requires a larger map size and longer computing time. However, the size and computing time of the feature-indexed map are less sensitive to the total distance of the map than those of the position-indexed map. For example, the map size for the unit distance of the PIM is 40.8 kB/m, and that of multiple feature-indexed maps is 1.36 kB/m. The computing time for the unit distance of the scanning method with PIM is 0.1147 ms/m, and that of multiple feature-indexed maps is 0.0025 ms/m.

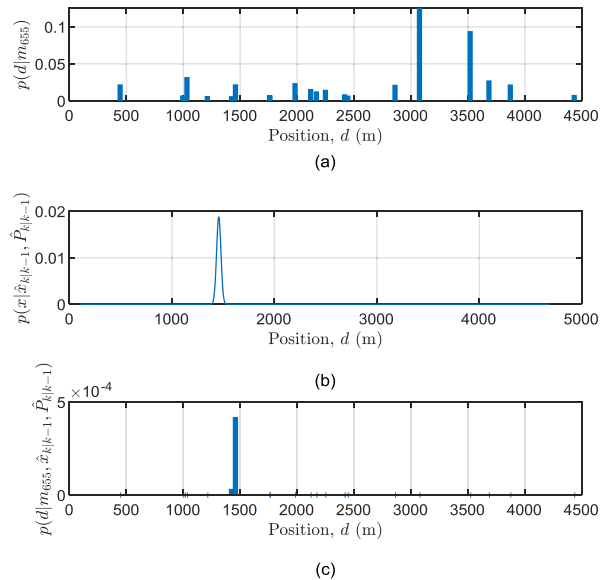


**FIGURE 18.** Concept of reflecting the vehicle dynamics into the position candidates: (a) the current measurement (position information of  $m_{655}$ ); (b) the expected position distribution based on the Kalman filter; and (c) the position information considering the expected position and the current measurement.

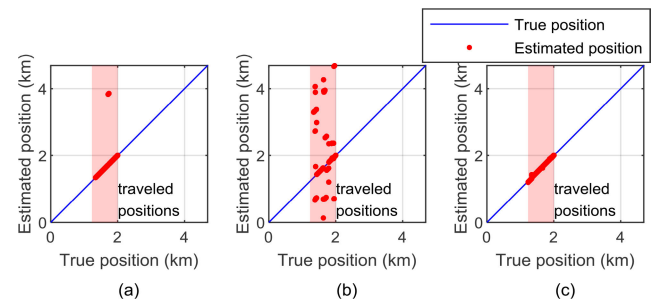


**FIGURE 19.** Effect of integration of the Kalman filter and a feature-indexed map: (a) scanning method with a position-indexed map of vertical shape; (b) scanning method with a position-indexed map of lateral shape; and (c) integration of the Kalman filter and a feature-indexed map.

Fig. 21 also shows the benefit of using multiple feature-indexed maps compared to the method with a single feature-indexed map. The spectrograms need to have a long-distance range and high overlap to improve the accuracy and resolution simultaneously with only a single map. Therefore, the map requires a huge size and long computing time. For example, a single feature-indexed map for 10000 meter-distance requires 130.68 MB and 0.1 seconds. On the other hand, multiple feature-indexed maps for the same total distance need 38.45 MB and 0.025 seconds. In other words, the positioning method based on multiple feature-indexed maps can increase the accuracy and resolution without using too large a map and too much computation.

Table 1 summarizes the contributions of the proposed methods. All non-GPS-based positioning methods require a map, and the problem is the map size and computational

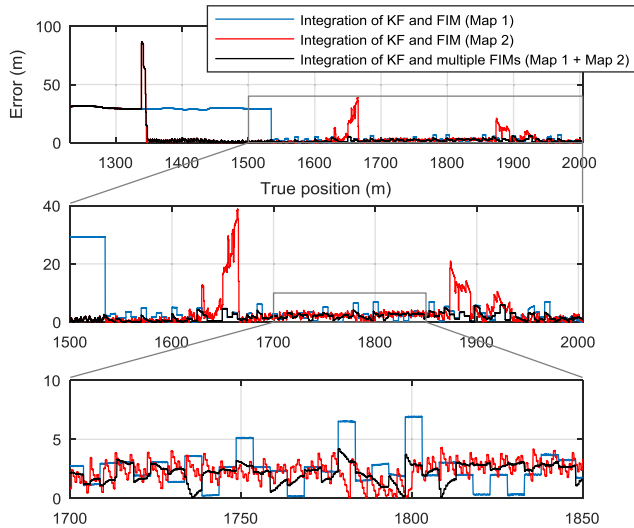


FIGURE 20. Effect of using multiple maps.

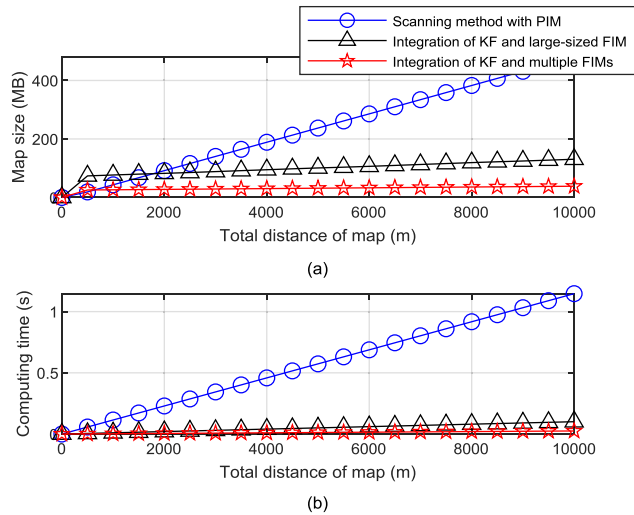


FIGURE 21. Map sizes and computing times of several methods that have the same resolution: (a) map size with respect to the total distance of map and (b) computing time with respect to the total distance of map.

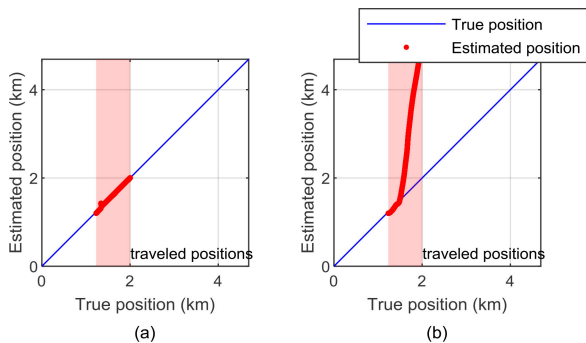


FIGURE 22. IMU-based positioning results: (a) proposed method and (b) dead reckoning (a typical method for inertial sensor-based positioning).

load. The proposed feature-indexed map reduces both map size and computing time because it stores the position with

TABLE 1. Summary of proposed methods' effects.

Effects	FIM	KF Integration	Multiple Maps	Note
Map size-reduction	O			Fig. 21 (a)
Computing time reduction	O			Fig. 21 (b)
Suppressed sudden position changes	O	O		Figs. 18, 19
Enabling the use of multiple measurements		O		Fig. 19
Simultaneous increase of accuracy and resolution w/o too large size and computational load	O		O	Figs. 20, 21

respect to features, whereas general maps store features with respect to positions, and its validation is shown in Fig. 21. The integration of the Kalman filter and the feature-indexed map suppresses sudden positioning changes, as shown in Figs. 18 and 19. The Kalman filter integration also improves the positioning accuracy by providing an integration framework of multiple measurements (estimated positions using vertical and lateral road shapes), as shown in Fig. 19. The positioning with multiple feature-indexed maps improves the positioning accuracy and resolution without a large increase of the map size and the computational load, as shown in Figs. 20 and 21. Finally, Fig. 22 shows that the proposed method eliminates the error accumulation, a chronic problem that prevents long time horizon application of the mainstream algorithm for inertial sensor-based positioning called dead reckoning. Therefore, the proposed positioning method can quickly identify the position of the vehicle with only an inertial sensor without error accumulation.

V. CONCLUSION

This paper presented an inertial sensor-based positioning method with no dead reckoning. Vertical and lateral road shapes can be used as features to identify positions on a road, but road shapes are not necessarily unique and do not vary monotonically. Therefore, we proposed a feature-indexed map and integrated the road shape-based positioning method with vehicle dynamics using a Kalman filter framework. The approach has several benefits, such as reduced map size, reduced computational load, increased accuracy, and the ability to use multiple maps.

One limitation is that the accuracy is a few meters, which is not as good as DGPS or RTK because characteristic features on the road may not exist every few centimeters. Another limitation is that the method is valid for one-dimensional localization. This method cannot identify the current lane unless maps for all lanes are available. However, the most substantial benefit of the proposed algorithm is that the required sensor is cost-effective, reliable, and robust to environmental changes. Therefore, this method would still be available even when wireless signals are blocked or optical sensors are malfunctioning because of severe weather conditions. Possible applications are the localization of public transportation running on an exclusive lane with a fixed route

and a backup for the localization of military vehicles on a battlefield where GPS is jammed and optical sensors cannot work because of smoke. In addition, the proposed method is scalable to the general non-GPS-based localization by constructing map structure in the feature domain using image-based features and definition of two-dimensional position probabilistic information.

## REFERENCES

- [1] T. Bamonte. (Jul. 24, 2013). *Autonomous Vehicles: Drivers for Change*. Roads Bridges. [Online]. Available: <https://www.roadbridges.com/autonomous-vehicles-drivers-change>
- [2] T. G. R. Reid, S. E. Houts, R. Cammarata, G. Mills, S. Agarwal, A. Vora, and G. Pandey, "Localization requirements for autonomous vehicles," *SAE Int. J. Connected Automated Vehicles*, vol. 2, no. 3, pp. 173–190, Sep. 2019, doi: [10.4271/12-02-03-0012](https://doi.org/10.4271/12-02-03-0012).
- [3] E. Yurtsever, J. Lambert, A. Carballo, and K. Takeda, "A survey of autonomous driving: Common practices and emerging technologies," *IEEE Access*, vol. 8, pp. 58443–58469, 2020, doi: [10.1109/ACCESS.2020.2983149](https://doi.org/10.1109/ACCESS.2020.2983149).
- [4] A. Chehri, N. Quadar, and R. Saadane, "Survey on localization methods for autonomous vehicles in smart cities," in *Proc. 4th Int. Conf. Smart City Appl.*, Casablanca, Morocco, Oct. 2019, pp. 1–6.
- [5] A. Kleusberg and R. B. Langley, "The limitations of GPS," *GPS World*, vol. 1, no. 2, pp. 50–52, Mar. 1990.
- [6] N. M. Drawil, H. M. Amar, and O. A. Basir, "GPS localization accuracy classification: A context-based approach," *IEEE Trans. Intell. Transp. Syst.*, vol. 14, no. 1, pp. 262–273, Mar. 2013, doi: [10.1109/TITS.2012.2213815](https://doi.org/10.1109/TITS.2012.2213815).
- [7] L. S. Monteiro, T. Moore, and C. Hill, "What is the accuracy of DGPS?" *J. Navigat.*, vol. 58, no. 2, pp. 207–225, Apr. 2005, doi: [10.1017/S037346330500322X](https://doi.org/10.1017/S037346330500322X).
- [8] M. E. Cannon, "High-accuracy GPS semikinematic positioning: Modeling and results," *Navigat.*, vol. 37, no. 1, pp. 53–64, Mar. 1990, doi: [10.1002/j.2161-4296.1990.tb01534.x](https://doi.org/10.1002/j.2161-4296.1990.tb01534.x).
- [9] H. Blomenhofer, G. W. Hein, E. T. Blomenhofer, and W. Werner, "Development of a real-time DGPS system in the centimeter range," in *Proc. IEEE Position, Location Navigat. Symp. (PLANS)*, Las Vegas, NV, USA, Apr. 1994, pp. 532–539.
- [10] C. Brenner, "Global localization of vehicles using local pole patterns," in *Proc. DAGM*, Jena, Germany, 2009, pp. 61–70.
- [11] A. Welzel, A. Auerswald, and G. Wanielik, "Accurate camera-based traffic sign localization," in *Proc. 17th Int. IEEE Conf. Intell. Transp. Syst. (ITSC)*, Qingdao, China, Oct. 2014, pp. 445–450.
- [12] B. Soheilani, X. Qu, and M. Bredif, "Landmark based localization: LBA refinement using MCMC-optimized projections of RJMCMC-extracted road marks," in *Proc. IEEE Intell. Vehicles Symp. (IV)*, Gothenburg, Sweden, Jun. 2016, pp. 940–947.
- [13] M. Sefati, M. Daum, B. Sondermann, K. D. Kreiskother, and A. Kampker, "Improving vehicle localization using semantic and pole-like landmarks," in *Proc. IEEE Intell. Vehicles Symp. (IV)*, Los Angeles, CA, USA, Jun. 2017, pp. 13–19.
- [14] V. Balali, A. Jahangiri, and S. G. Machiani, "Multi-class US traffic signs 3D recognition and localization via image-based point cloud model using color candidate extraction and texture-based recognition," *Adv. Eng. Inform.*, vol. 32, pp. 263–274, Apr. 2017, doi: [10.1016/j.aei.2017.03.006](https://doi.org/10.1016/j.aei.2017.03.006).
- [15] X. Qu, B. Soheilani, and N. Paparoditis, "Landmark based localization in urban environment," *ISPRS J. Photogramm. Remote Sens.*, vol. 140, pp. 90–103, Jun. 2018, doi: [10.1016/j.isprsjprs.2017.09.010](https://doi.org/10.1016/j.isprsjprs.2017.09.010).
- [16] Y. Li, W. Wang, S. Tang, D. Li, Y. Wang, Z. Yuan, R. Guo, X. Li, and W. Xiu, "Localization and extraction of road poles in urban areas from mobile laser scanning data," *Remote Sens.*, vol. 11, no. 4, p. 401, Feb. 2019, doi: [10.3390/rs11040401](https://doi.org/10.3390/rs11040401).
- [17] E. Javanmardi, Y. Gu, M. Javanmardi, and S. Kamijo, "Autonomous vehicle self-localization based on abstract map and multi-channel LiDAR in urban area," *IATSS Res.*, vol. 43, no. 1, pp. 1–13, Apr. 2019, doi: [10.1016/j.iatssr.2018.05.001](https://doi.org/10.1016/j.iatssr.2018.05.001).
- [18] A. Schaefer, D. Büscher, J. Vertens, L. Luft, and W. Burgard, "Long-term vehicle localization in urban environments based on pole landmarks extracted from 3-D lidar scans," *Robot. Auto. Syst.*, vol. 136, Feb. 2021, Art. no. 103709, doi: [10.1016/j.robot.2020.103709](https://doi.org/10.1016/j.robot.2020.103709).
- [19] L. Li, M. Yang, L. Weng, and C. Wang, "Robust localization for intelligent vehicles based on pole-like features using the point cloud," *IEEE Trans. Automat. Sci. Eng.*, early access, Jan. 17, 2021, doi: [10.1109/TASE.2020.3048333](https://doi.org/10.1109/TASE.2020.3048333).
- [20] D. Jie, J. Masters, and M. Barth, "Lane-level positioning for in-vehicle navigation and automated vehicle location (AVL) systems," in *Proc. IEEE ITSC*, Washington, WA, USA, Oct. 2004, pp. 35–40.
- [21] Z. Tao, P. Bonnifait, V. Fremont, and J. Ibanez-Guzman, "Mapping and localization using GPS, lane markings and proprioceptive sensors," in *Proc. IROS*, Tokyo, Japan, Nov. 2013, pp. 406–412.
- [22] M. Schreiber, C. Knoppel, and U. Franke, "LaneLoc: Lane marking based localization using highly accurate maps," in *Proc. IEEE Intell. Vehicles Symp. (IV)*, Gold Coast, QLD, Australia, Jun. 2013, pp. 449–454.
- [23] D. Gruyer, R. Belaroussi, and M. Revilloud, "Map-aided localization with lateral perception," in *Proc. IEEE Intell. Vehicles Symp. Proc.*, Dearborn, MI, USA, Jun. 2014, pp. 674–680.
- [24] M. Schlingelhof, D. Betaille, P. Bonnifait, and K. Demasure, "Advanced positioning technologies for co-operative systems," *IET Intell. Transp. Syst.*, vol. 2, no. 2, pp. 81–91, May 2008, doi: [10.1049/iet-its:20070046](https://doi.org/10.1049/iet-its:20070046).
- [25] I. Skog and P. Handel, "In-car positioning and navigation technologies—A survey," *IEEE Trans. Intell. Transp. Syst.*, vol. 10, no. 1, pp. 4–21, Feb. 2009, doi: [10.1109/TITS.2008.2011712](https://doi.org/10.1109/TITS.2008.2011712).
- [26] N. Piasco, D. Sidibé, C. Demonceaux, and V. Gouet-Brunet, "A survey on visual-based localization: On the benefit of heterogeneous data," *Pattern Recognit.*, vol. 74, pp. 90–109, Feb. 2018, doi: [10.1016/j.patcog.2017.09.013](https://doi.org/10.1016/j.patcog.2017.09.013).
- [27] F. de Ponte Müller, "Survey on ranging sensors and cooperative techniques for relative positioning of vehicles," *Sensors*, vol. 17, no. 2, p. 271, Jan. 2017, doi: [10.3390/s17020271](https://doi.org/10.3390/s17020271).
- [28] S. Kuutti, S. Fallah, K. Katsaros, M. Dianati, F. McCullough, and A. Mouzakitis, "A survey of the state-of-the-art localization techniques and their potentials for autonomous vehicle applications," *IEEE Internet Things J.*, vol. 5, no. 2, pp. 829–846, Apr. 2018, doi: [10.1109/JIOT.2018.2812300](https://doi.org/10.1109/JIOT.2018.2812300).
- [29] F. B. Günay, E. Öztürk, T. Çavdar, Y. S. Hanay, and A. U. R. Khan, "Vehicular ad hoc network (VANET) localization techniques: A survey," *Arch. Comput. Methods Eng.*, vol. 28, no. 4, pp. 3001–3033, Jun. 2021, doi: [10.1007/s11831-020-09487-1](https://doi.org/10.1007/s11831-020-09487-1).
- [30] K. Wei-Wen, "Integration of GPS and dead-reckoning navigation systems," in *Proc. VNIS*, Troy, MI, USA, Oct. 1991, pp. 635–643.
- [31] J. A. Farrell, T. D. Givargis, and M. J. Barth, "Real-time differential carrier phase GPS-aided INS," *IEEE Trans. Control Syst. Technol.*, vol. 8, no. 4, pp. 709–721, Jul. 2000, doi: [10.1109/87.852915](https://doi.org/10.1109/87.852915).
- [32] J. Ryu and J. C. Gerdes, "Integrating inertial sensors with global positioning system (GPS) for vehicle dynamics control," *J. Dyn. Syst., Meas., Control*, vol. 126, no. 2, pp. 243–254, 2004, doi: [10.1115/1.1766026](https://doi.org/10.1115/1.1766026).
- [33] A. Dean, R. Martini, and S. Brennan, "Terrain-based road vehicle localization using particle filters," *Veh. Syst. Dyn.*, vol. 49, no. 8, pp. 1209–1223, Jul. 2011, doi: [10.1080/00423114.2010.493218](https://doi.org/10.1080/00423114.2010.493218).
- [34] E. I. Laftchiev, C. M. Lagoa, and S. N. Brennan, "Vehicle localization using in-vehicle pitch data and dynamical models," *IEEE Trans. Intell. Transp. Syst.*, vol. 16, no. 1, pp. 206–220, Feb. 2015, doi: [10.1109/TITS.2014.2330795](https://doi.org/10.1109/TITS.2014.2330795).
- [35] P. K. Vemulapalli, A. J. Dean, and S. N. Brennan, "Pitch based vehicle localization using time series subsequence matching with multi-scale extrema features," in *Proc. ACC*, San Francisco, CA, USA, Jun. 2011, pp. 2405–2410.
- [36] T. Li, M. Yang, H. Li, L. Deng, and C. Wang, "A terrain-based vehicle localization approach robust to braking," *IEEE Trans. Intell. Transp. Syst.*, vol. 20, no. 8, pp. 2923–2932, Aug. 2019, doi: [10.1109/TITS.2018.2869475](https://doi.org/10.1109/TITS.2018.2869475).
- [37] J. Gim and C. Ahn, "Ground vehicle localization based on inertial measurement signals," in *Proc. ICCAS*, Busan, South Korea, Oct. 2015, pp. 1775–1779.
- [38] H. Ahmed and M. Tahir, "Terrain-based vehicle localization using low cost MEMS-IMU sensors," in *Proc. IEEE 83rd Veh. Technol. Conf. (VTC Spring)*, Nanjing, China, May 2016, pp. 1–5.
- [39] J. Gim and C. Ahn, "IMU-based virtual road profile sensor for vehicle localization," *Sensors*, vol. 18, no. 10, p. 3344, Oct. 2018, doi: [10.3390/s18103344](https://doi.org/10.3390/s18103344).
- [40] M. Zasadzinski, D. Mehdi, and M. Darouach, "Recursive state estimation for singular systems," in *Proc. Amer. Control Conf.*, Boston, MA, USA, Jun. 1991, pp. 2850–2851.

- [41] M. Darouach, M. Zasadzinski, A. B. Onana, and S. Nowakowski, "Kalman filtering with unknown inputs via optimal state estimation of singular systems," *Int. J. Syst. Sci.*, vol. 26, no. 10, pp. 2015–2028, Oct. 1995, doi: [10.1080/00207729508929152](https://doi.org/10.1080/00207729508929152).
- [42] J. MacQueen, "Some methods for classification and analysis of multivariate observations," in *Proc. Symp. Math. Statist. Prob.*, Berkeley, CA, USA, 1967, pp. 281–297.
- [43] R. J. Meinhold and N. D. Singpurwalla, "Understanding the Kalman filter," *Amer. Statistician*, vol. 37, no. 2, pp. 123–127, May 1983, doi: [10.1080/00031305.1983.10482723](https://doi.org/10.1080/00031305.1983.10482723).
- [44] H. A. P. Blom and Y. Bar-Shalom, "The interacting multiple model algorithm for systems with Markovian switching coefficients," *IEEE Trans. Autom. Control*, vol. 33, no. 8, pp. 780–783, Aug. 1988, doi: [10.1109/9.1299](https://doi.org/10.1109/9.1299).
- [45] E. Mazor, A. Averbuch, Y. Bar-Shalom, and J. Dayan, "Interacting multiple model methods in target tracking: A survey," *IEEE Trans. Aerosp. Electron. Syst.*, vol. 34, no. 1, pp. 103–123, Jan. 1998, doi: [10.1109/7.640267](https://doi.org/10.1109/7.640267).
- [46] Y. Ruan and L. Hong, "Use of the interacting multiple model algorithm with multiple sensors," *Math. Comput. Model.*, vol. 44, nos. 3–4, pp. 332–341, Aug. 2006, doi: [10.1016/j.mcm.2006.01.020](https://doi.org/10.1016/j.mcm.2006.01.020).
- [47] Z. He, X. Bu, H. Yang, and Y. Song, "Interacting multiple model cubature Kalman filter for geomagnetic/infrared projectile attitude measurement," *Measurement*, vol. 174, Apr. 2021, Art. no. 109077, doi: [10.1016/j.measurement.2021.109077](https://doi.org/10.1016/j.measurement.2021.109077).



**JUHUI GIM** (Student Member, IEEE) received the B.S. and Ph.D. degrees in mechanical engineering from Pusan National University, Busan, Republic of Korea, in 2015 and 2021, respectively.

She is currently a Postdoctoral Researcher at the Research Institute of Mechanical Technology, Pusan National University. Her research interests include estimation, localization, autonomous driving control, and hybrid power control based on deep learning.



**CHANGSUN AHN** (Member, IEEE) received the B.S. and M.S. degrees from Seoul National University, Seoul, South Korea, in 1999 and 2005, respectively, and the Ph.D. degree from the University of Michigan, Ann Arbor, in 2011, all in mechanical engineering.

He is currently an Associate Professor at Pusan National University, South Korea. His research interests include automotive control/estimation. Recently, he has focused on autonomous vehicle control.

• • •